CONFERENCE PRE-PRINT

DYNAMIC EVOLUTION OF PELLET FUELING FROM ABLATION CLOUD TO REHEAT MODE IN HELIOTRON J

S. KADO, S. INAGAKI, A. IWATA, F. KIN, S. KOBAYASHI, T. MIZUUCHI, S. KONOSHIMA, H. OKADA, T. MINAMI, K. NAGASAKI Institute of Advanced Energy, Kyoto University Uji, Kyoto, Japan Email: kado@iae.kyoto-u.ac.jp

G. MOTOJIMA

National Institute for Fusion Science, Toki, Gifu, Japan SOKENDAI (The Graduate University for Advanced Studies) Toki, Gifu, Japan

R. MATSUTANI, C. FENG, K. OGIHARA, T. KAWAMUKAI, F. CAI, A. MATSUYAMA, Y. NAKAMURA, A. ISHIZAWA

Graduate School of Energy Science, Kyoto University, Uji, Kyoto, Japan

T. SHIKAMA

Graduate School of Engineering, Kyoto University Katsura, Kyoto, Japan

S. OHSHIMA University of California, Irvine, California, U.S.A

Abstract

We investigate the impact of small hydrogen pellet injection on plasma fueling and confinement dynamics in Heliotron J. A comprehensive diagnostic suite—including two-dimensional Stark broadening spectroscopy, event-triggered Thomson scattering, EUV spectroscopy, and AXUV detectors—was employed to resolve the ablation, homogenization, and reheat phases. The 2D imaging of the H_{β} line reveals a spherical neutral cloud and an elongated plasmoid stretching along magnetic field lines. Following ablation, density profiles evolve from hollow to peaked, implying an inward pinch after flux-surface homogenization. Concurrently, impurity emissions recorded via EUV and AXUV diagnostics display characteristic transitions among ionization states, consistent with a "reheat mode" that helps the plasma surpass ECH cutoff density. These findings elucidate the coupling between pellet ablation, impurity dynamics, and heating schemes, and offer new insight into optimizing pellet fueling strategies in fusion-relevant magnetic confinement devices.

1. INTRODUCTION

Hydrogen pellet injection is recognized as an effective fueling method for fusion-relevant magnetic confinement devices. To date, pellet fueling experiments have been conducted in a variety of devices, including tokamaks, stellarators/heliotrons, and other magnetic confinement systems. One of the most important results in pellet-fueled plasmas is the attainment of high-density regimes that exceed the Greenwald density limit in tokamaks [1] or surpass the ISS04 scaling law in stellarators and heliotrons [2].

Improvements in confinement have not been limited to large-scale devices; medium-sized helical systems such as TJ-II have also demonstrated clear enhancements in performance [3]. In Heliotron J, which has a size comparable to TJ-II, a compact pellet injector has been constructed and operated [4]. Optimization studies concerning pellet size, injection velocity, and related parameters have been carried out. Compared with larger machines such as a the large helical device (LHD) or the Wendelstein 7-X (W7-X), the required injection speed is significantly lower in Heliotron J. Fuel deposition profiles inferred from an H α detector array have been compared with the results of the simulation code ABLATE [5]. These efforts underscore the need for a systematic approach that bridges modeling and experimental measurement, including sensitivity to different heating schemes.

However, the interaction between a solid hydrogen pellet and the bulk plasma during fueling is inherently dynamic and complex. Optimally designing pellet fueling scenarios requires a detailed understanding of both microscopic atomic processes and macroscopic transport phenomena. In this light, we have focused on the development of diagnostics capable of directly observing the pellet fueling dynamics.

The remainder of this paper is organized as follows. In Section 2, we review the ablation dynamics and fueling mechanisms of cryogenic hydrogen in magnetically confined high-temperature plasmas, with emphasis on diagnostic challenges. Section 3 presents a classification of the plasma responses observed following pellet injection in Heliotron J. Section 4 describes the diagnostic systems developed to interrogate each phase of the fueling process. Section 5 provides the experimental results, including 2D ablation mapping, homogenization behavior, and reheat phenomena. Section 6 discusses the validity, limitations, and interpretative constraints of the measurements. Finally, Section 7 summarizes the principal findings and outlines avenues for future work.

2. ABLATION PROCESSES AND DIAGNOSITIC CHALLENGES

The pellet ablation process generally proceeds through three distinct phases [6]:

- 1) Ablation and Plasmoid Formation: The solid hydrogen pellet ablates, producing a neutral cloud that subsequently ionizes into a high-density, low-temperature plasma known as a plasmoid.
- 2) Plasmoid Expansion and Homogenization: The plasmoid evolves and expands along magnetic flux surfaces, thereby distributing the fuel.
- 3) Fuel Deposition and Plasma Profile Reconstruction: The injected fuel assimilates into the bulk plasma, modifying the density profile and completing the fueling process.

In Phase 1), the penetration depth and/or deposition profile of the injected pellet can be inferred from the Balmer- α (H $_{\alpha}$) emission line intensity (656.28 nm) and compared with simulation models, such as the neutral-gas-shielding

(NGS) model [7]. Atomic emission is primarily determined by the neutral density, the background electron density and temperature. To evaluate the density of the plasmoid—that is, the cold, high-density plasma cloud—a spectroscopic approach is required, typically via Stark broadening of emission line spectra, typically of Balmer- β (H $_{\beta}$) line (486.1 nm). For large devices such as LHD, plasmoid parameters have been measured using the intensity ratio obtained from two interference filters with different passbands (narrow: 5 nm; broad: 20 nm) [8]. In our medium-sized device, however, the observed spectral broadening is significantly narrower than the range resolvable by a combination of interference filters

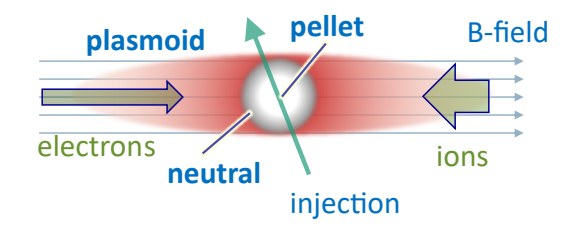


FIG. 1 Schematic illustration of the pellet ablation cloud.

with differing passbands—hence, the intensity-ratio approach based on such filters becomes intrinsically inapplicable. Although local thermal equilibrium (LTE) may be assumed in the early ablation stage, its validity is expected to weaken as Phase 1) progresses toward Phase 2) [9].

In Phase 2), plasmoid homogenization can be detected on the flux surface where the pellet ablates, forming a "cold pulse ring." As the pellet penetrates, the ring appears to expand inward across the minor radius. This inwardly expanding structure manifests as a low-temperature, high-density "disk" surrounding the plasma center, which may retain its pre-injection parameters. Conventional Thomson scattering diagnostics, typically operating at repetition rates of ~100 Hz [10], are insufficient to capture this transient ablation event. To obtain time-resolved snapshots, we developed an event-triggered Thomson scattering system, using H_{α} emission as the trigger signal.

In Phase 3), conventional plasma diagnostics can be applied. In particular, dynamic profile changes can be monitored using an AXUV diode detector array. Sixteen line-integrated signals are reconstructed into local spatial emission profiles via Abel inversion. It must be noted, however, that the detector cannot distinguish between radiating species. Consequently, variations in emission profiles may result from changes in the density profile, impurity radiation, or both. Furthermore, plasma collapse is readily induced, as a single pellet typically delivers 5–10 times more particles than are contained in the entire target plasma. Therefore, proper interpretation of the

radiation process requires consideration of both impurity species as radiators and the electron temperature.

3. TEMPORAL EVOLUTION OF THE PELLET-FUELLED PLASMAS IN HELIOTRON J

Heliotron J is a medium-sized helical device with a major radius R=1.2 m, a minor radius $a\sim0.2$ m, and a typical magnetic field strength of B=1.25 T. Plasma is initiated using electron cyclotron heating (ECH) with a 70 GHz gyrotron, typically delivering 190–280 kW of power in this experiment. Additional heating can be provided by neutral beam injection (NBI). A compact pellet injector with a barrel diameter of 0.6–1.2 mm has been developed for Heliotron J [4]. The pellet diameter, corresponding to the barrel size, is selected according to plasma conditions and heating power. Under the present experimental conditions, a diameter of 0.7 mm has been determined to be optimal.

Fig. 2 shows typical temporal evolutions of the reheat phenomena, categorized into different types. In this case, NBI was used only for its beam conditioning and can therefore be neglected in the analysis. Pellet injection was also performed in NBI-sustained plasmas and in plasmas heated by combined ECH+NBI.

Immediately after pellet injection, three distinct responses of the stored energy (W_p) , measured using a diamagnetic loop, were observed. **Type A** exhibited clear plasma cooling followed by recovery to a higher-density state. This behavior is reminiscent of the so-called "reheat" mode [11]. Following the reheat phase, the subsequent decay of W_p typically followed two pathways: a mild decay (**Type B**) or a rapid decay (**Type C**).

4. DIAGNOSTIC SYSTEM RELEVANT TO EACH PHASES

4.1. Ablation phase

Viewing chords used to measure the ablation cloud are illustrated in Fig. 3. A 16-channel H_{α} array system, consisting of interference filters and avalanche photodiodes, is employed to measure pellet penetration depth.

For the ablation phase, we developed a two-dimensional (2D) fast visible spectrometer that combines spectral, imaging, and high-speed capabilities. Emission collected along the pellet trajectory is imaged onto a fiber-optic bundle arranged in a 12×12 channel 2D imaging array, which is then reformatted into a one-dimensional (1D) array along the spectrometer entrance slit.

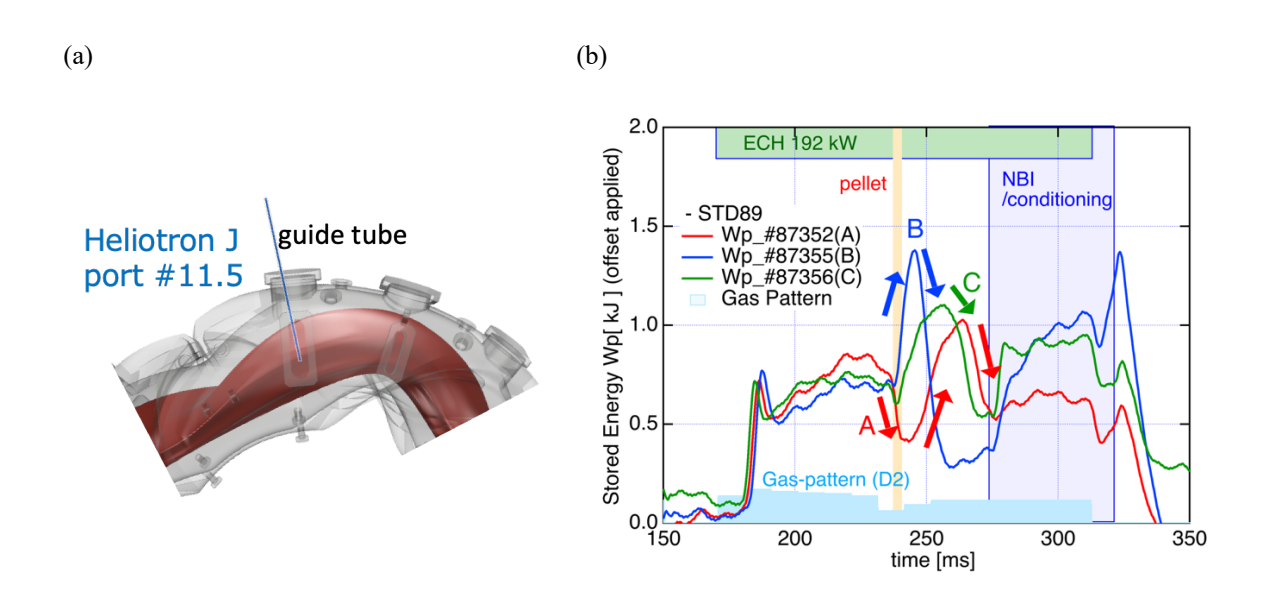


FIG. 2 Typical patterns of the "reheat" phenomenon. (a) Pellet injection port; (b) Type A–C reheat responses. The pellet is injected into an ECH plasma with reduced gas fueling to avoid radiation collapse.

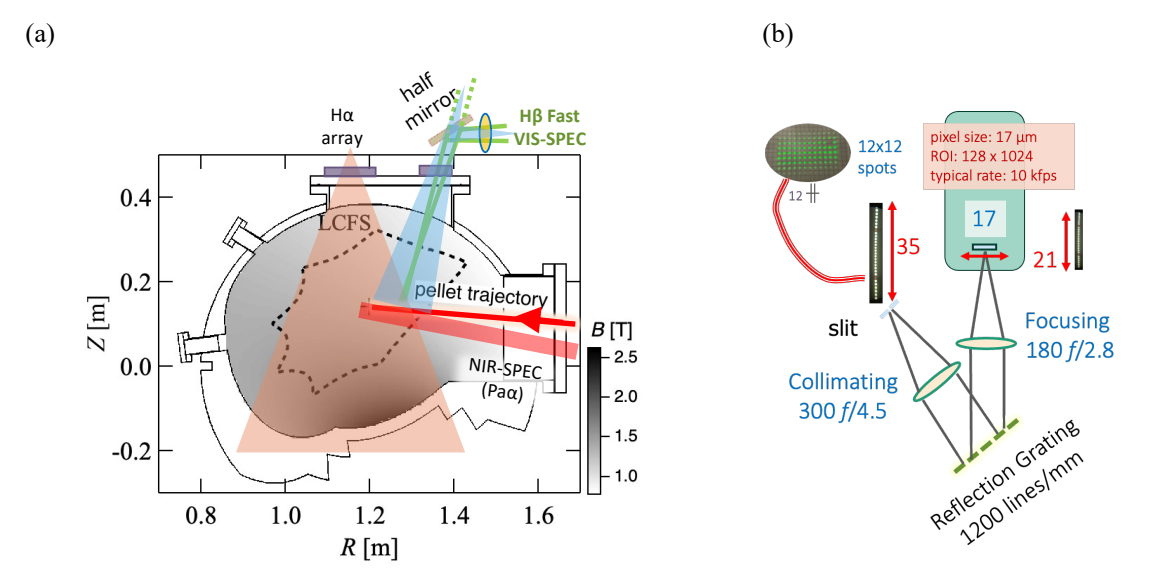


FIG. 3(a) Schematic view of the spectroscopy systems for the pellet ablation cloud. The H\alpha array is used to measure penetration depth. A near-infrared (NIR) spectrometer is employed for Paschen-series line profiles and intensity ratios. Emission from the pellet trajectory is divided between the fast visible spectrometer developed in this work and a high-dispersion NIR spectrometer for Zeeman spectroscopy.

(b) Schematic view of the optical configuration of the spectrometer.

Commercial photographic lenses (Nikon) with focal lengths of 300 mm (f/4.5) and 180 mm (f/2.8) were used as the collimator and focusing optics, respectively, yielding $0.6 \times$ reduced image magnification with an effective aperture of 67 mm. This configuration enables an acceptance of 35 mm slit height at the detector, corresponding to 21 mm in the vertical dimension. A reflection grating with 1200 grooves/mm was employed, providing a reciprocal linear dispersion (RLD) of 3.50 nm/mm for the H β line at 486.13 nm.

A high-speed camera (Photron FASTCAM APX-RS) allows frame rates of up to 10,000 fps for a rectangular region of interest (ROI) of 128 pixels in wavelength and 1024 pixels along the slit direction. With a vertical dimension of 17.4 mm (corresponding to 1024 pixels), a slit height of 29 mm is achievable, enabling the simultaneous recording of 126 fibers out of 151 (including seven alignment fibers). The spectroscopic data from each fiber can then be remapped to its corresponding plasma position [12].

4.2. Homogenization Phase: Event-Triggered Thomson Scattering System

For the homogenization phase, we developed an event-triggered Thomson scattering system. The timing sequence of this system is illustrated in Fig. 4. At the start of the experimental sequence ("zero second"), the trigger resets the laser system's timer counter and synchronizes it with the plasma discharge time.

Two laser systems operating at 50 Hz are available, enabling 100 Hz operation for regular pulsing [10]. In event-triggered mode, the lasers remain on standby until a trigger signal is received. The trigger is generated when the specified H_{α} signal exceeds a preset threshold. The lasers then fire after a user-defined delay plus a jitter of approximately 80 μ s.

Since the optimal interval between flashlamp ignition and Q-switch actuation (for maximal amplifier gain) is fixed at 250 μs , the minimum total delay from event onset is about 330 μs . Consequently, while the system cannot capture the earliest phase of ablation, it can effectively probe the later stage.

4.3. Profile reconstruction phase

In this phase, conventional diagnostic systems can be applied. A useful tool is the 16-channel AXUV photodiode detector

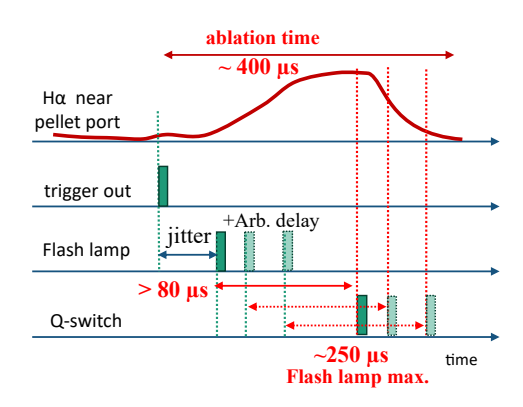


FIG. 4 Timing sequence of the event-triggered Thomson scattering.

array, which measures total radiation power in the range of 0.0124–1100 nm (1.1 eV–100 keV). The corresponding measurement chords are illustrated in Fig. 5. The spatial radiation profile can be determined using the Abel inversion technique.

For impurity line spectra, an extra-ultraviolet (EUV) spectrometer equipped with a shot-by-shot spatial scanning system is available. However, due to the limited reproducibility of pellet-injected plasmas, reconstructing spatial profiles from scanned line-integrated spectra is not feasible. Instead, the viewing chord is fixed at the plasma center throughout the experiment, enabling monitoring of the temporal evolution of various impurity species and charge states, such as C, O, and Fe.

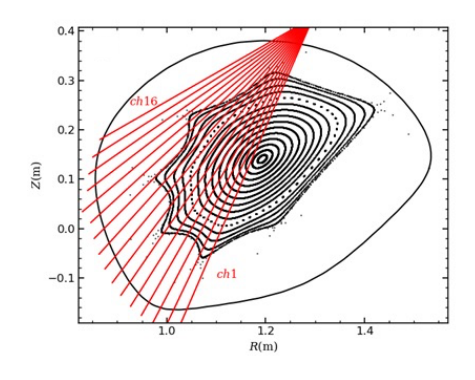


FIG. 5 Measurement chords of the AXUV detector array.

5. RESULTS

5.1. Ablation phase

The results of the two-dimensional (2D) mapping of measured intensity and density derived from Stark broadening are shown in Fig. 6. The ablation time was approximately 0.4 ms, during which H_{β} spectra were detected in four frames corresponding to a fragment of the pellet. The upper images represent emission intensity, primarily attributed to the neutral cloud. The lower images show pixel-by-pixel spectral fitting results, yielding Stark broadening profiles. The maximum densities, which typically coincide with the brightest pixels in the upper maps, were 0.21, 0.63, 1.00, and 1.35 \times 10²¹ m⁻³. These values are about two orders of magnitude lower than those observed in LHD.

It can be seen that the plasmoid elongates along the magnetic field direction, marking the onset of the homogenization process. From the temporal evolution of the 2D images, the arrival position of the brightest core

can be deduced. In total, 165 pellet shots—including ECH, NBI, and ECH+NBI heated plasmas—were conducted in FY2024 and classified accordingly. Fig. 7 shows the distribution of the arrival points. Fig. 7(a) presents the raw mapping, while Fig. 7(b) shows the rearrangement based on the departure from the designed injection path (x-axis) and the distance to the magnetic axis (y-axis).

From the histogram of these shots, generally the reheat type A appears when the pellet reaches deep into the core, close to the magnetic axis, while the Type C appears when it ablated out relatively sharrow region. Departure seemed to be more obvious for the NBI heated plasmas. Details are still under discussion.

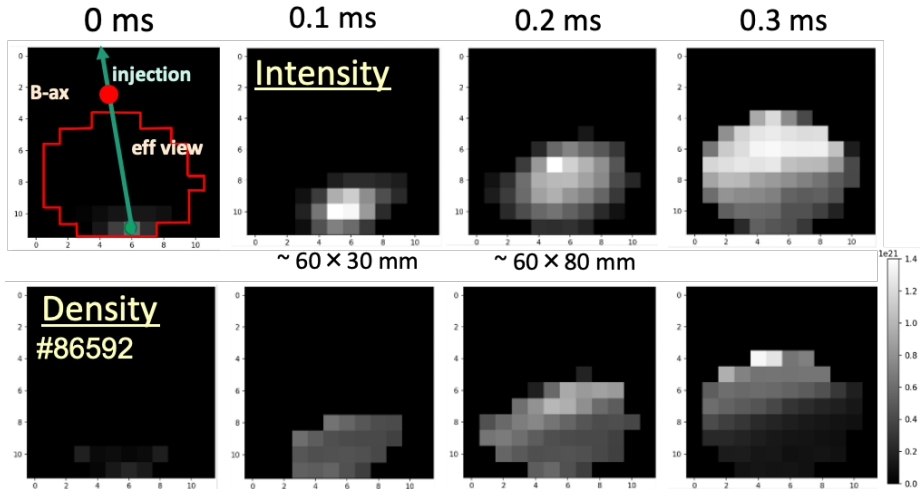


FIG. 6 Two-dimensional images of the neutral cloud (upper) and the plasmoid density (lower) viewed from the top.

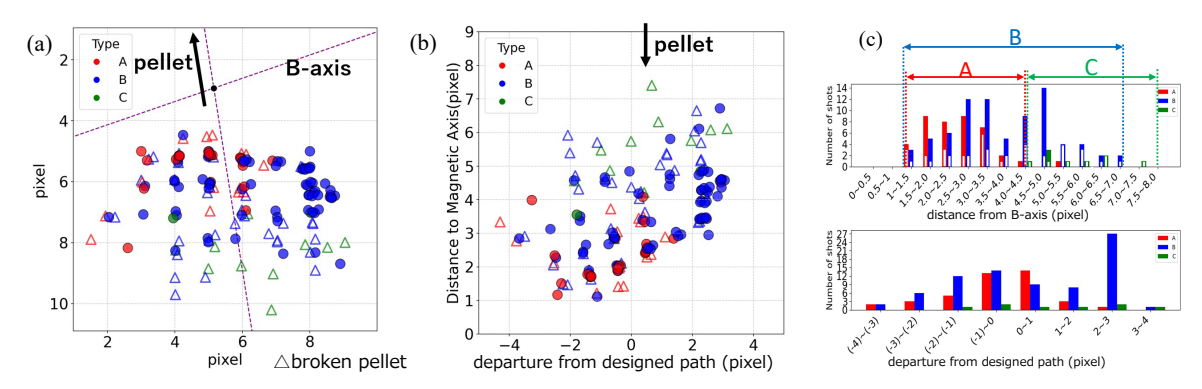


FIG. 7 Mapping of the arrival points of the ablation cloud. (a) Raw data. (b) Rearrangement with respect to the magnetic axis and designed injection path. (c) Histogram of penetration positions. Colors indicate the type of reheat, and open squares represent fragmented pellets.

5.2. Homogenization Phase: Observation of the Cold Ring

Fig. 8 shows the temporal evolution of electron temperature (T_e) and electron density (n_e) in a pellet-fueled, ECH-only heated plasma. Conventional Thomson scattering diagnostics were used to measure the target plasma parameters at 230 ms (shot #79541). Subsequently, the operating mode was switched to event-triggered acquisition. The H α signal indicated that ablation began at 239.9 ms, which we define as time zero for the ablation event. The pellet was likely fully ablated (i.e. the ablation process completed) at around 0.5 ms (shots #79544 and #79546). We adjusted the laser timing so that Laser #1 recorded data at 0.5 ms and 0.6 ms after trigger for shots #79544 and #79546, respectively; the interval between Laser #1 and Laser #2 was set to 0.1 ms. Thus, we obtained T_e and n_e of the bulk plasma at 0.5, 0.6, 1.1, and 1.2 ms after the trigger (data at 1.2 ms are omitted here).

The baseline (pre-pellet) profile exhibited a Gaussian-like $T_{\rm e}$ distribution and a hollow $n_{\rm e}$ structure, typical of ECH-heated plasmas. Upon pellet injection, we observed a pronounced electron cooling in the periphery while maintaining a relatively hot core at 0.5 ms. In contrast, $n_{\rm e}$ increased modestly, appearing as though a "cold-density ring" had formed around the hot core. We interpret this as a direct snapshot of the homogenization process [6]. This ring rapidly progressed inward, forming a "disk," and the central density rose to 4.6×10^{19} m⁻³ within 1 ms — a rate much faster than typical particle transport timescales.

To date, only a limited number of event-triggered data sets are available, because this diagnostic mode is incompatible with standard operation. Nevertheless, these

preliminary results demonstrate the formation of a transient cold ring structure, offering key insight into the early stage of plasmoid homogenization.

5.3. Profile Reconstruction Phase: Reheat Phenomena

The response of bulk plasma parameters, Phase 3), following pellet ablation is typically manifested as a cold pulse, during which emission from highly charged impurity ions abruptly vanishes or is suppressed (depending on the perturbation magnitude), while emissions from lower-charged ions increase. Subsequently, the plasma transitions into a reheat-like behavior.

Fig. 9 illustrates the temporal evolution of impurity line spectra in the EUV region. A comparison is made between two cases: pellet injection during the NBI-only heating phase (#86675) and pellet injection while ECH is superposed on NBI heating (#86676). During operation,

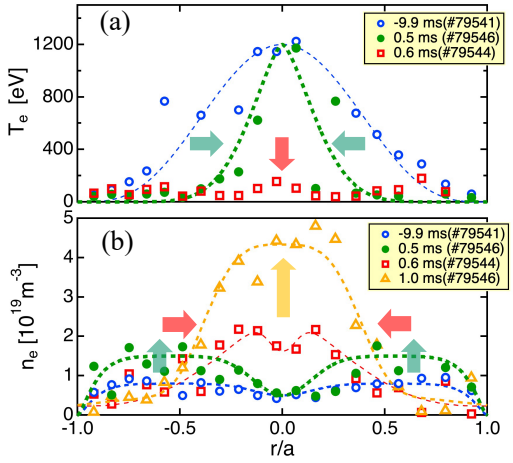


FIG. 8 Electron temperature (a) and density(b) profiles of the target plasma before pellet injection (-9.9 ms), during the pellet ablation (0.5 ms) and immediately after the ablation (0.6 ms from the Hα trigger ON)). n_e at 1.0 ms is added [shot#79541-79546] [13].

gas puffing is increased to approach the threshold for radiation collapse, as evidenced by the enhancement of the central AXUV signal after the reheat event. In the case with ECH applied, collapse was prevented. After injection, O V emission slightly decreased, while C III emission increased, consistent with a cold pulse. As the plasma evolves, radiators progressively shift from lower to higher charge states (e.g., from C III to O V and Fe XV/XVI). Cooling is observed in the latter half of the reheat phase, as seen in the decline of Fe XV and Fe XVI emissions.

A few milliseconds later, emission from the highly charged ions reappears, exceeding pre-ablation levels and correlating with the rise in stored energy W_p . This trend is also evident in the AXUV detector signals, which show that, after ablation, the dominant radiation region moves rapidly from the plasma edge to the core [14]. A simplified transport analysis using n_e and T_e profiles from Thomson scattering suggests the presence of an inward particle pinch.

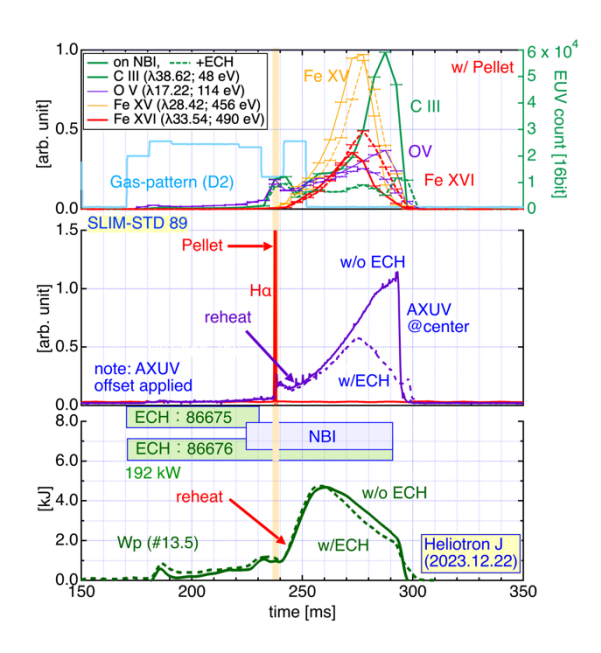


FIG. 9 Temporal evolution of the stored energy Wp and EUV impurity line spectra, annotated by wavelength and ionization energy.

The magnitude of reheat appears to depend on the heating scheme (ECH and/or NBI), heating power, and additional gas fueling which supplements recycling from the chamber wall. Understanding the mechanisms underlying the reheat mode and impurity dynamics is essential for achieving high-performance plasmas. In particular, ECH appears to serve a dual role: maintaining electron temperature and influencing radiator species peaking, possibly by expelling highly charged ions, as indicated by reductions in both O V and C III.

6. DISCUSSION

The densities obtained via this spectrometer agree with those we previously reported using two different types of spectrometers — high-dispersion [15] and low-dispersion [16] — applied to time- and space-averaged NIR Pa α lines. By fitting the calculated spectral line shapes for given T_c and n_c [17], we derived empirical calibration curves to estimate the plasmoid density from the measured Stark widths for visible H $_{\beta}$ and near-infrared Paschen- α (Pa $_{\alpha}$) lines [16]:

$$n_e = 1.74 \times 10^{22} \times \text{FWHM}^{1.44} \quad (\text{H}_{\beta}; 486.13 \text{ nm})$$
 (1)

$$n_e = 2.32 \times 10^{21} \times \text{FWHM}^{1.49}$$
 (Pa_{\alpha}; 1875.13 nm) (2)

It is notable that the H_{β} line would only exhibit a full width at half maximum (FWHM) of approximately 1 nm even when the plasmoid density is as high as 1.74 x 10^{22} m⁻³.

During the homogenization process, plasmoids may be subjected to various driving forces. In fact, experimental penetration depths sometimes deviate from model predictions. A high-speed camera (Photron FASTCAM SA5), operating at 100,000 frames per second, captured fluctuations in emission intensity from the ablation cloud. The observed rotational motion in the $E \times B$ drift direction around the pellet trajectory along magnetic field lines [18] likely reflects an early stage of plasmoid homogenization.

In helical devices, the magnetic field geometry along the pellet's path can be complex and varies among devices or injection ports. Therefore, the magnitude and direction of curvature drift or ∇B drift may also be intricate. Two-dimensional mapping of both emission intensity and plasmoid density has the potential to visualize the plasmoid's travel direction during homogenization.

7. SUMMARY AND FUTURE PROSPECTS

In this work, we succeeded in capturing the intensity, density, and trajectory of the ablation cloud, providing a nearly complete view of the ablation process—typically lasting around 0.4 ms per pellet fragment. For the homogenization phase, we developed an event-triggered Thomson scattering system that enables tracking changes in plasma profiles at an arbitrary delay (≥ 0.33 ms) after the ablation event, using the H α emission signal as a trigger. Using these relatively novel diagnostics, we have probed the dynamic behavior of pellet-fueled plasmas. High-speed Stark broadening spectroscopy proved highly effective for extracting plasmoid properties such as trajectory, velocity, penetration depth, density, and morphology. The event-driven Thomson scattering system offers access to the homogenization phase of the ablation process. Meanwhile, the AXUV array enables reconstruction of impurity emission profiles, and EUV spectroscopy can help identify the radiating species.

Going forward, key challenges remain in elucidating the interplay among heating schemes, reheat behavior, and pellet ablation properties. In particular, understanding how different heating methods (e.g. ECH, NBI) influence the reheat mode and impurity dynamics will be essential for optimizing pellet fueling strategies in fusion devices. Further improvements in time resolution, diagnostic accuracy, and multi-channel synergy will aid in advancing toward high-performance, stable plasma regimes.

ACKNOWLEDGEMENTS

This research was supported by HONMAMON co-creative research program between HORIBA and Kyoto University (HM002 to S. Kado), JSPS KAKENHI Grant Number JP19K03803 (to G. Motojima), 25K07261 (to S. Kado), and NIFS Collaboration Research program (NIFS16KUHL073) to G. Motojima.

REFERENCES

- [1] P.T. Lang et al., Nucl. Fusion **58** 036001(2018).
- [2] R. Sakamoto et al Nucl. Fusion 49 085002(2019).
- [3] I. García-Cortés et al., Phys. Plasmas 30, 072506 (2023).
- [4] G. Motojima et al., Rev. Sci. Instrum. 87, 103503 (2016).
- [5] G. Motojima, et al., 2019, Plasma. Phys. Control. Fusion., 61, (2019) 075014.
- [6] A. Matsuyama, et al., Plasma Phys. Control. Fusion 54 (2012) 035007.
- [7] Y. Nakamura et al., Nucl. Fusion 26 907(1986).
- [8] G. Motojima et al., Rev. Sci. Instrum. 83, 093506 (2012).
- [9] A. Iwata, et al, Plasma and Fusion Research 19, 1402017 (2024).
- [10] N. Kenmochi, et al., Rev. Sci. Instrum. 85, 11D819 (2014).
- [11] S. Morita *et al.*, Proc. 14th Int. Conf. Plasma Physics and Controlled Nuclear Fusion Research 1992, Würzburg, Vol.2, p.515 (1992).
- [12] S. Kado, et al., 2023, Proc. 49th EPS conference, Bordeaux, P4.040.
- [13] R. Matsutani, et al., 2023, Proc. 49th EPS conference, Bordeaux, P4.043.
- [14] K,Ogihara et al., Rev Sci Instrum 84, 083504 (2025).
- [15] M. Murakumo et al., Rev. Sci. Instrum. 96, 043501 (2025).
- [16] A. Iwata, et al, Rev Sci Instrum. 93, 113537 (2022).
- [17] C. Stehlé and R. Hutcheon, Astron. Astrophys., Suppl. Ser. 140, 93–97 (1999).
- [18] S. Ohshima, et al., Scientific Reports, 12, 14204(2022).